Eur. Phys. J. A (2022) 58:217
https://doi.org/10.1140/epja/s10050-022-00877-6

THE EUROPEAN PHYSICAL JOURNAL A

Regular Article - Experimental Physics

Prompt emission of γ-rays and neutrons from the fast neutron induced fission of ^{232}Th at neutron energies near and above the fission threshold

Sukanya De[1,2], **R. G. Thomas**[1,2,a], **G. Mishra**[1], **A. Mitra**[1], **Ajay Kumar**[1]

[1] Nuclear Physics Division, Bhabha Atomic Research Centre, Trombay, Mumbai 400085, India
[2] Homi Bhabha National Institute, Anushaktinagar, Mumbai 400094, India

Received: 10 August 2022 / Accepted: 31 October 2022

Communicated by R. Janssens

Abstract Measurements of prompt fission γ-rays and neutrons emitted in the fast neutron induced fission of ^{232}Th have been carried out at incident neutron energies of 1.5 MeV, 2.1 MeV and 2.8 MeV. The γ-rays were recorded using two $CeBr_3$ scintillation detectors in coincidence with a twin section fission trigger ionisation chamber while the neutrons were detected using two EJ301 liquid scintillation detectors. The energy spectra of γ-rays were obtained after unfolding the detected pulse height spectrum using the response matrix of the $CeBr_3$ detectors. The extracted prompt fission γ-ray spectra for ^{232}Th(n,f) when compared with the existing data of ^{252}Cf(sf),^{239}Pu(n,f) and ^{238}U(n,f), showed noticeably lower intensity of photons at energies less than 0.7 MeV. No significant excitation energy dependence of the spectral characteristics of prompt fission γ-ray spectra for ^{232}Th(n,f) has been observed. The time-of-flight spectra measured using EJ301 detectors with respect to the twin section fission trigger chamber were used to determine the prompt fission neutron energy spectra at all the three incident neutron energies mentioned above. The measured spectra were then fitted using Maxwell and Watt parametrizations to derive the average prompt fission neutron energy. It is found that GEF describes neutron data well, but fails to corroborate with gamma data.

1 Introduction

Improved understanding of prompt fission gamma and neutron emission helps us to gain insight about the energy partitioning in fission process, the re-organization of nuclear matter around scission and the subsequent de-excitation process of the fission fragments [1–3]. The excitation energy sharing mechanism between the fission fragments, the fragment angular momentum generation process and their interdependence is still a matter of intense investigation [4–8]. It is generally understood that once fission occurs, during the fragment de-excitation process, neutrons are primarily emitted until the excitation energy of the fragments nears the neutron separation energy [9]. Photons are emitted once the neutron emission is hindered and, in general, account for the loss of the fragment angular momentum. The transition from neutron emission to photon emission in the fission fragment de-excitation is still not well understood [10]. Most of the recently developed models such as GEF [11], FREYA [12], CGMF [13], FIFRELIN [14], are data driven and rely on experimental data to benchmark their calculations. It is also important to note that a comparison of the results obtained from various measurements of the prompt fission gamma spectra (PFGS) and prompt fission neutron spectra (PFNS) exhibits variations from one another in the actinide region [15–21]. Measurement of the PFGS and PFNS for fast neutron induced fission of actinides has also gained renewed interest due to its importance in the development of GEN-IV fast reactors and Accelerator Driven Systems [22,23]. While the PFGS is required for accurately estimating the gamma heating in reactor cores [24], the PFNS play an important role in the accurate predictions of nuclear criticality using neutron transport codes and other properties of nuclear systems [25]. It is also worth noting that only limited measurements exist for the prompt γ-rays and neutrons emitted in the fast neutron induced fission of certain actinides, particularly ^{232}Th.

In the present work, we report the measurements carried out for the PFGS and PFNS in the neutron induced fission of ^{232}Th at near and above the fission threshold. The paper is organised as follows: in Sect. 2, details of the experimental set-up are described. In Sect. 3, data analysis which involves

[a] e-mail: rgthomas@barc.gov.in (corresponding author)

Published online: 10 November 2022

simulation of the response functions for the Cerium Bromide ($CeBr_3$) detectors and the EJ301 detectors using GEANT4 are described. The experimental results and their comparison with existing data and model predictions are also presented in the sub-sections. Finally, the summary is given in the last section.

2 Experiment

The experiment was performed at the Folded Tandem Ion Accelerator (FOTIA) facility, BARC, Mumbai. A schematic of the experimental setup is shown in Fig. 1. Proton beam with energies 3.5, 4.1 and 4.8 MeV were bombarded on a natural Li metallic foil target of thickness ~ 4.0 mg/cm^2. Quasi mono-energetic neutrons of 1.5, 2.1 and 2.8 MeV respectively were obtained using the ^{7}Li(p,n)^{7}Be reaction. A twin section fission trigger detector, shown in Fig. 2, covering a solid angle of nearly 4π was used to detect the fission fragments. It contains a cathode and an anode in each section, made of copper plated G-10 discs of diameter 7.5 cm, which were separated by 2.0 mm thick Teflon spacer rings. Self supporting ^{232}Th foils of thickness ~ 2.0 mg/cm^2 and dimensions ~ 1.0 cm $\times$ 1.0 cm were pasted onto the cathodes of each of the two sections of the fission trigger detector. The anode plates were given a bias of 400 V and the cathode plate was kept at the ground potential. Each of the two sections acts as a separate fission trigger detector, thereby enhancing the fission detection efficiency. This configuration also ensures that the energy loss in the ^{232}Th foil, even for the heaviest fragments, will introduce little or no bias in the detection efficiency of the fragments. The fission fragments deposit a fraction of their energies within the trigger chamber by generating electron-ion pairs which give rise to an electrical signal. A typical fission fragments energy loss spectrum produced in the twin section fission trigger detector is shown in Fig. 3. Timing signal from the fission detector acts as the trigger for recording the neutron Time-of-Flight (TOF) spectrum as well as the γ-ray pulse height spectrum.

The γ-rays were measured using two 1.5" $\times$ 1.5" cylindrical $CeBr_3$ detectors [26], placed at angles of 33° and 58° with respect to the proton beam direction and at distances of 20 cm and 22 cm from the fission target. Negative voltages of 760 V and 800 V were applied to the PMT of the $CeBr_3$ detectors. The energy calibration of the detectors were performed using standard radioactive sources; namely ^{22}Na, ^{60}Co and ^{137}Cs. A non-linearity of less than $\sim$3% is observed in our current measurements, which is comparable to the value obtained in our earlier work for the same set of $CeBr_3$ detectors [26]. The threshold of both the $CeBr_3$ detectors was 190 keV. In order to reduce the contribution due to background γ-rays, a shielding arrangement was made using lead bricks.

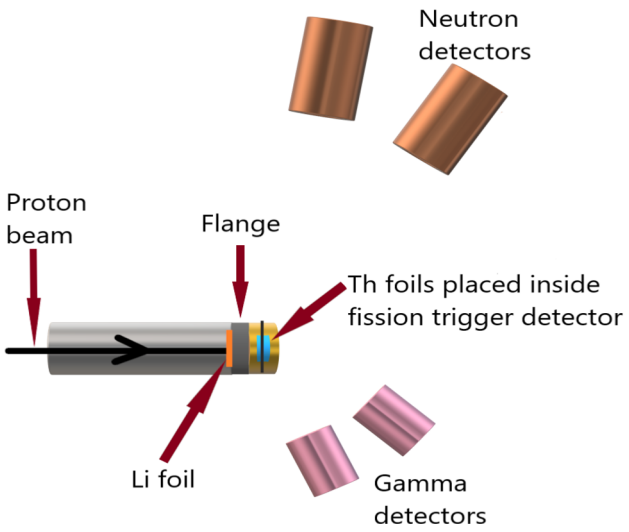

Fig. 1 A schematic of the experimental setup

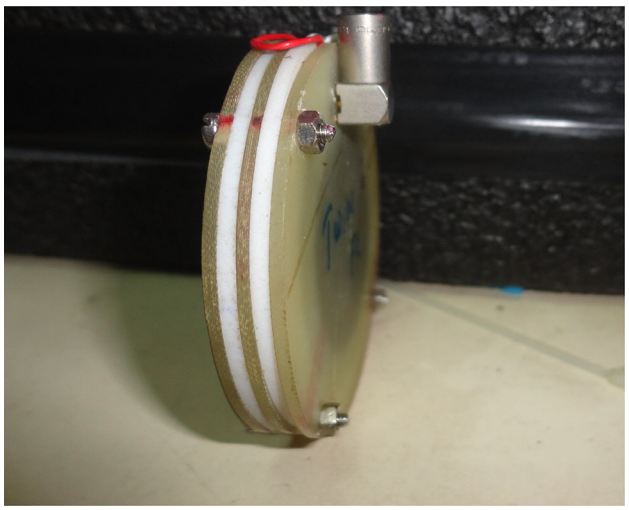

Fig. 2 The twin section fission trigger detector, used for detection of fission fragments. Self supporting ^{232}Th foils of thickness ~ 2.0 mg/cm^2 and dimensions ~ 1.0 cm $\times$ 1.0 cm were pasted onto the cathodes of each of the two sections of the detector

Two EJ301 liquid scintillation detectors (12.7 cm diameter and 5.0 cm thick) were placed at angles 55° and 80° with respect to the proton beam direction and at distances of 77.5 cm and 82.5 cm from the fission target. Bias of -1300 V was applied to both the neutron detectors. The detectors were calibrated using the Compton edges of ^{60}Co, ^{137}Cs and ^{22}Na γ-ray sources. The threshold of the neutron detectors were 66 keV electron equivalent (keVee) (370 keV neutron energy) and 47 keVee (280 keV neutron energy). The anode signals from EJ301 detectors were processed through the MPD-4 (Mesytec) module [27] to obtain the pulse shape discrimination, pulse height and timing information. A VME-based data acquisition system was used to record the data in list-mode as described in [28].

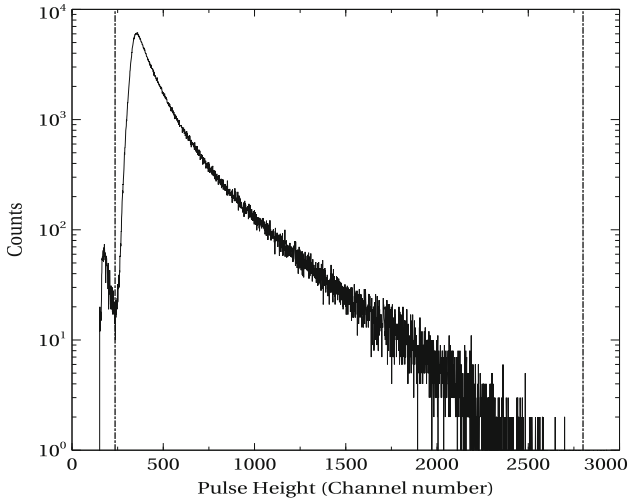

Fig. 3 Fission energy loss spectrum produced in the twin section fission trigger detector. The region enclosed by red dot-dashed vertical lines indicate the fission events

Table 1 The average energy of the neutrons produced (<E_n>) along with the energy spread (ΔE_n) for the three incident proton energies (E_p) and the excitation energy of the compound nucleus (E^*_{CN})

E_p (MeV)	<E_n> (MeV)	ΔE_n (keV)	E^*_{CN} (MeV)
3.5	1.47	157	6.26
4.1	2.08	138	6.86
4.8	2.80	140	7.56

3 Analysis and results

3.1 Determination of average energy of the neutrons incident on the ^{232}Th foils

The distance between the primary Li target and the ^{232}Th foils is ~5.5 mm. The neutron flux was ~3×10^6 neutrons/cm^2/s on the ^{232}Th target for an incident 3.5 MeV proton beam current of ~30 nA. The energy distribution of the neutrons produced from the ^{7}Li(p,n)^{7}Be reaction [29] was calculated using EPEN [30] for the three incident proton energies. The average energy of the incident neutrons (<E_n>) along with the energy spread (ΔE_n) and the excitation energy of the compound nucleus (E^*_{CN}) are tabulated in Table 1.

3.2 Prompt fission gamma spectra (PFGS)

The ^{252}Cf(sf) PFGS has been already extensively studied and thereby serve as a benchmark for our PFGS extraction procedure. Hence, in order to validate the data analysis procedure, the PFGS from the ^{252}Cf(sf) source was measured using the same experimental setup. The coincident TOF spectra of the γ-rays (top) and its 1-D projection (bottom) are shown for

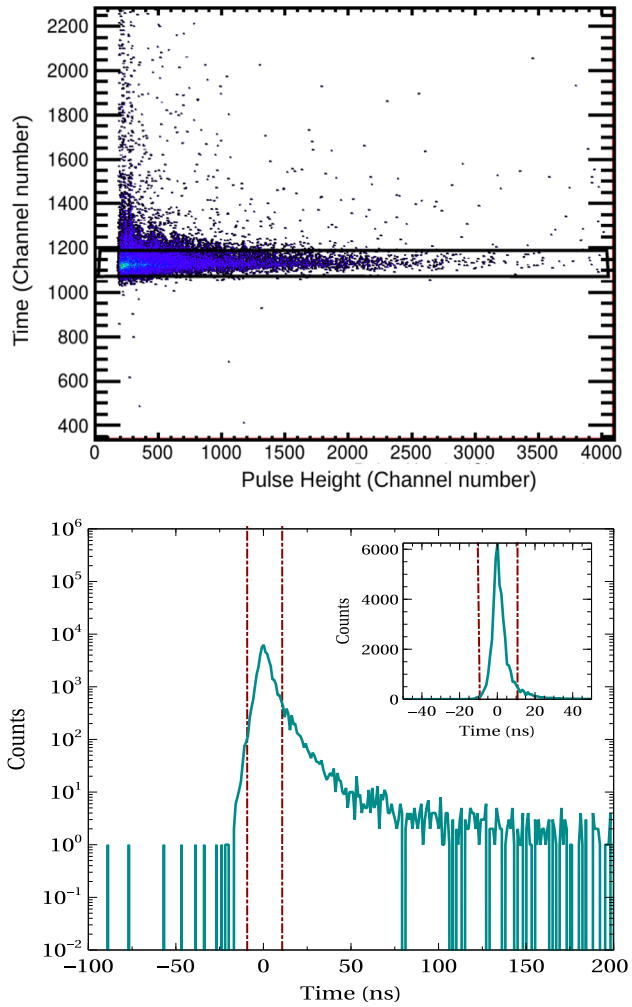

Fig. 4 The 2-D plot showing TOF versus Pulse Height spectrum (top) recorded in one of the γ-ray detectors in coincidence with the twin section fission trigger detector and its 1-D projection (bottom) in the case of ^{252}Cf(sf). Plot in linear scale is shown in the inset

^{252}Cf(sf) and ^{232}Th($n_{1.5\ MeV}$,f) in Figs. 4 and 5, respectively. The coincidence prompt time window used in the analysis is ±10 ns as shown by red lines in Figs. 4 (bottom) and 5 (bottom). Firstly, we selected another time window of ± 10 ns beyond the prompt gamma region so that only the random background contributes in that region. Then, we subtracted this background spectrum from the total prompt spectrum recorded in the gamma detectors to obtain the background corrected spectrum.

The measured spectrum needs to be unfolded with the help of the response matrix **R** of the detecting system to extract the emission spectrum. In order to obtain **R** the exact geometry including the detectors and Pb shielding assembly are modelled in GEANT4 [31] as shown in Fig. 6. The validation of the geometry used in simulations is carried out by matching the simulation results with the experimental data of two standard γ-ray sources ^{137}Cs and ^{60}Co mea-

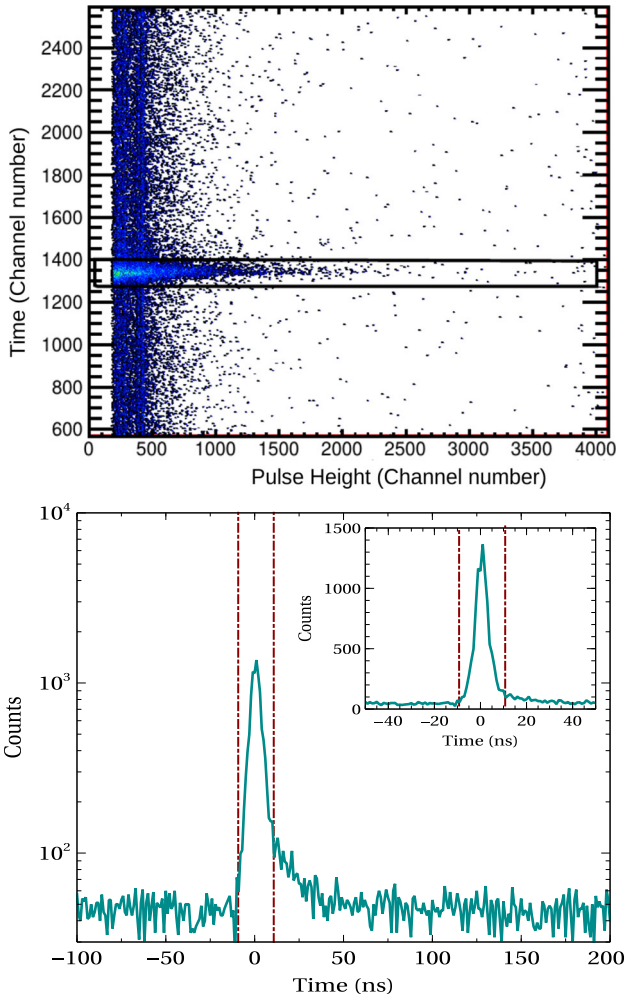

Fig. 5 The 2-D plot showing TOF versus Pulse Height spectrum (top) recorded in one of the γ-ray detectors in coincidence with the twin section fission trigger detector and its 1-D projection (bottom) in the case of ^{232}Th($n_{1.5\ MeV}$,f). Plot in linear scale is shown in the inset

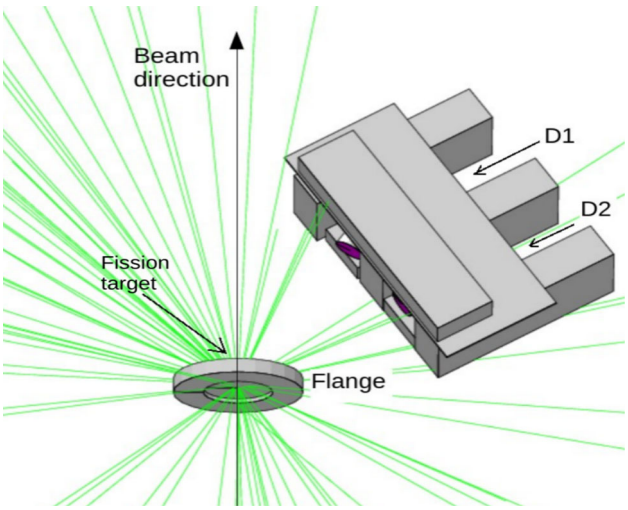

Fig. 6 Experimental setup modelled in GEANT4

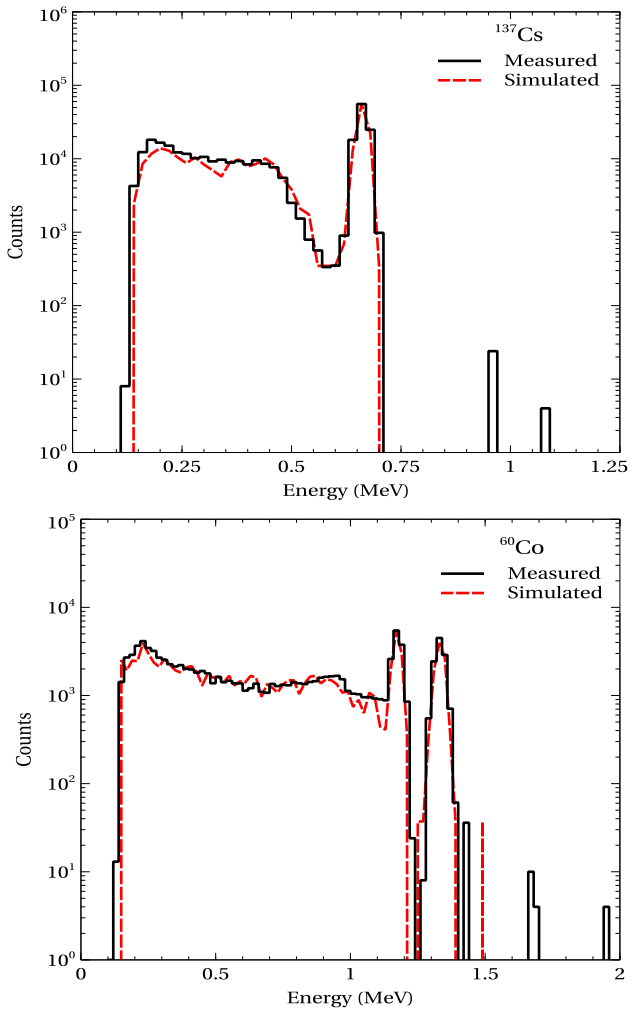

Fig. 7 Simulated (red line) and experimentally measured (black line) spectrum for ^{137}Cs (top) and ^{60}Co (bottom) γ-ray sources

sured using the same experimental setup. The Monte Carlo simulations were carried out using GEANT4 version 10.6 with the standard EM physics list. The simulated and experimentally measured spectra for ^{137}Cs and ^{60}Co are shown in Fig. 7. It can be seen that the simulation reproduces the experimental data very well even in the low energy region where back-scattering from the shielding materials are also present. Response matrices for both the $CeBr_3$ detectors were obtained in this configuration using the simulation performed using GEANT4 by incorporating the parameters obtained by fitting the energy spectrum of ^{60}Co and ^{137}Cs γ-ray sources. The simulations were carried out at each energy step for 10^7 events each for incident γ-rays of energies ranging from 0 to 10 MeV in steps of 20 keV and the energy deposited within each bin was generated. A 3-D plot of the response matrix thus obtained for one of the $CeBr_3$ detectors is shown in Fig. 8.

Though various unfolding algorithms have been developed in order to obtain the emission PFGS, recent results

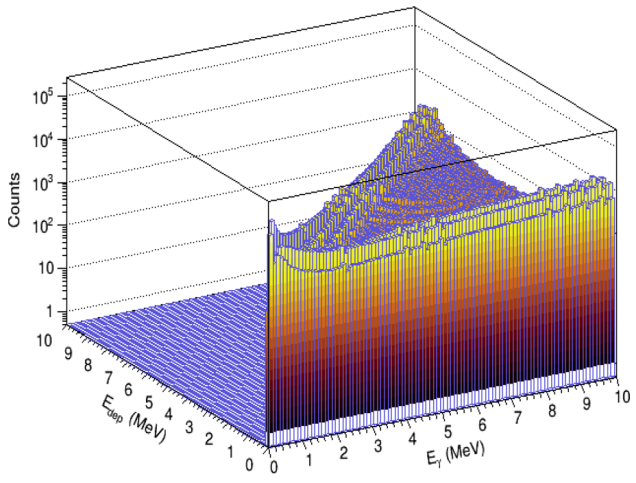

Fig. 8 Response matrix of one of the $CeBr_3$ detectors simulated using GEANT4

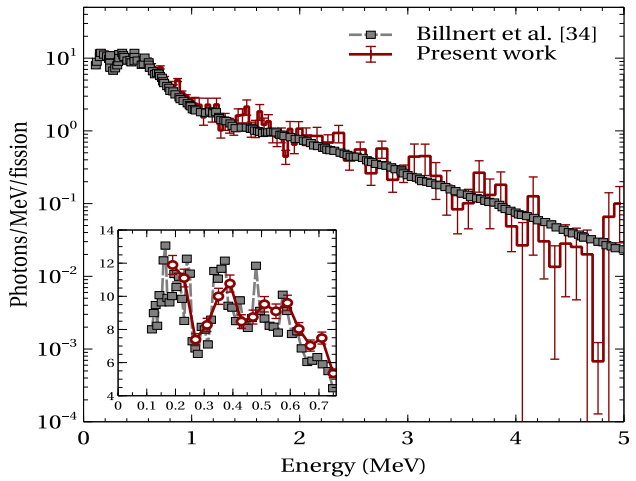

Fig. 9 Comparison of the PFGS of ^{252}Cf(sf) obtained from the present work and measurements from Billnert et al. [32]. The low energy region (<0.8 MeV) is shown in the inset

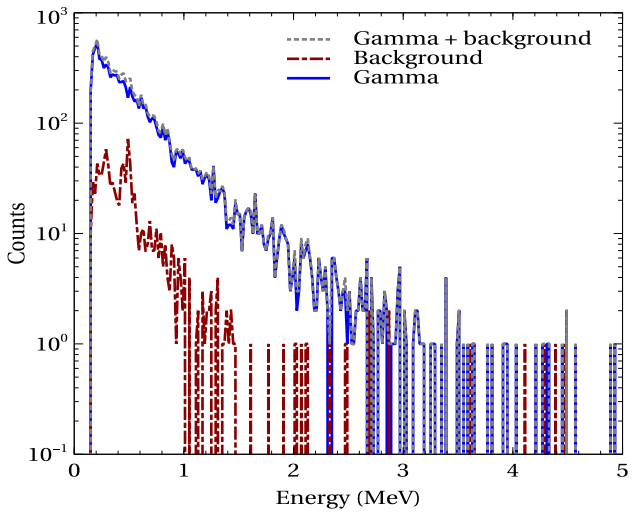

Fig. 10 Measured γ-ray spectrum (before unfolding) obtained using one of the $CeBr_3$ detectors, the background spectrum and the background subtracted measured spectrum of ^{232}Th($n_{1.5\ MeV}$,f)

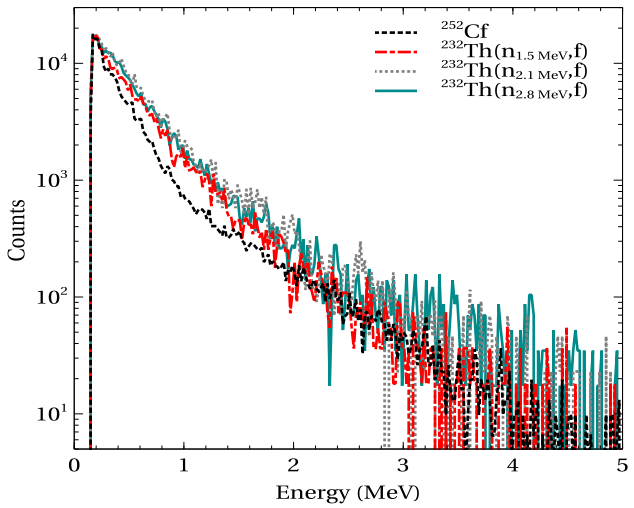

Fig. 11 Comparison of the background subtracted measured γ-ray spectrum (before unfolding) for ^{252}Cf(sf) and ^{232}Th(n,f) at the three incident neutron energies

from the data of Qi et al. [33] depict that the iteration method generates more stable results as compared to other techniques for spectra with limited statistics, which is particularly relevant for the PFGS measurements in the case of fast neutron induced fission of actinides. The measured ^{252}Cf(sf) spectrum recorded in each of the individual $CeBr_3$ detectors was unfolded separately with the help of GRAVEL algorithm (iterative method) [28,34] using the corresponding response matrix of each detector. The final emission spectrum is then obtained by adding the emission spectra extracted for both the detectors which is normalized to the number of fission events. The comparison of the obtained PFGS with the results of Billnert et al. [32] is shown in Fig. 9. As can be seen from the figure, the peak positions as well as the intensities obtained from the present work agree quite well with Billnert et al. [32] though the data below 0.19 MeV is not available due to the higher electronic threshold in our measurements.

Following the successful validation of the procedure in the case of ^{252}Cf(sf), the PFGS for ^{232}Th(n,f) were obtained by unfolding the measured spectra at 1.5, 2.1 and 2.8 MeV incident neutron energies by the same procedure. The background subtracted measured spectrum before unfolding obtained in one of the gamma detectors for ^{232}Th(n,f) at incident neutron energy of 1.5 MeV is shown in Fig. 10 by a blue solid line. The background subtracted measured spectra before unfolding for ^{232}Th(n,f) at the three incident neutron energies along with that of ^{252}Cf(sf) are shown in Fig. 11. For easy visualization, the spectra in Fig. 11 have been normalised to the maximum value at E = 0.19 MeV in order to

compare the variation of the γ-ray spectral shapes for the different cases before unfolding.

The unfolded PFGS for all the three energies for ^{232}Th(n,f) are shown in Fig. 12a–c. The spectra in the low energy range are shown (maximum up to 1.5 MeV) as insets. The bin widths are chosen based on the available statistics and are kept at 40 keV for low energy γ-rays (<2 MeV) and at 100 keV for spectra above 2 MeV. Also shown in Fig. 12a–c are the predictions of the GEF model. It is quite evident that there is wide discrepancy between the experimental data and the GEF model predictions of the PFGS in ^{232}Th(n,f) at all the incident neutron energies. The average γ-ray energy, $<E_\gamma>$, in the region of 0.19–5.0 MeV obtained from the present experiment as well as the GEF model predictions are tabulated in Table 2.

Error in the PFGS contributed by the unfolding technique is estimated as follows: The γ-ray measured spectra obtained from the ^{252}Cf(sf) recorded in the gamma detectors were simulated using GEANT4-FREYA [12] for similar statistics as in our experimental case and unfolded using the GRAVEL algorithm. The deviation obtained from repeated such simulations and corresponding unfolding, provided the estimate of the error involved in the deconvolution technique. The statistical uncertainties, propagated through the γ-ray deconvolution algorithm have also been taken into account.

Figure 13 shows a comparison of the unfolded γ-ray spectra in the low energy range, obtained from the present experiment. Figure 14 shows a comparison of the unfolded γ-ray spectra in the low energy range, obtained from the ^{252}Cf(sf) [32], ^{238}U($n_{1.9MeV}$,f) and ^{239}Pu($n_{1.8\ MeV}$,f) [35] and ^{232}Th(n,f) at the three incident neutron energies. In the low-energy region, the PFGS is mostly dominated by discrete (mainly quadrupole) transitions, typically observed between low-lying rotational energy levels in fission fragments. These low-energy contributions are superimposed on a continuous spectrum of statistical γ-rays, which are mainly E1 transitions. The latter cover a wide range of energies from a few tens of keV up to 10 MeV. In the simplest description of low-energy fission of actinides, the heavy nucleus breaks apart into two smaller fragments of unequal mass at the scission point. The pre-neutron heavy fission fragment yield is strongly peaked near $A_H \sim 140$ and the corresponding peak in the light fragment yield is $A_L \sim A_0 - A_H$ where A_0 is the mass of the fissioning nucleus [36]. As the fissioning systems are different, the fragment population, especially the lighter fragments, is different for the ^{252}Cf(sf), ^{239}Pu(n,f), ^{238}U(n,f) and ^{232}Th(n,f) systems. This difference may manifest in the PFGS as seen in Fig. 14. However, rigorous modelling of characteristic gamma emission is required to quantitatively understand the PFGS in the low energy region. It is also worth mentioning that other than GEF, the models FREYA and CGMF are yet to incorporate ^{232}Th (n, f) in their list of available reactions.

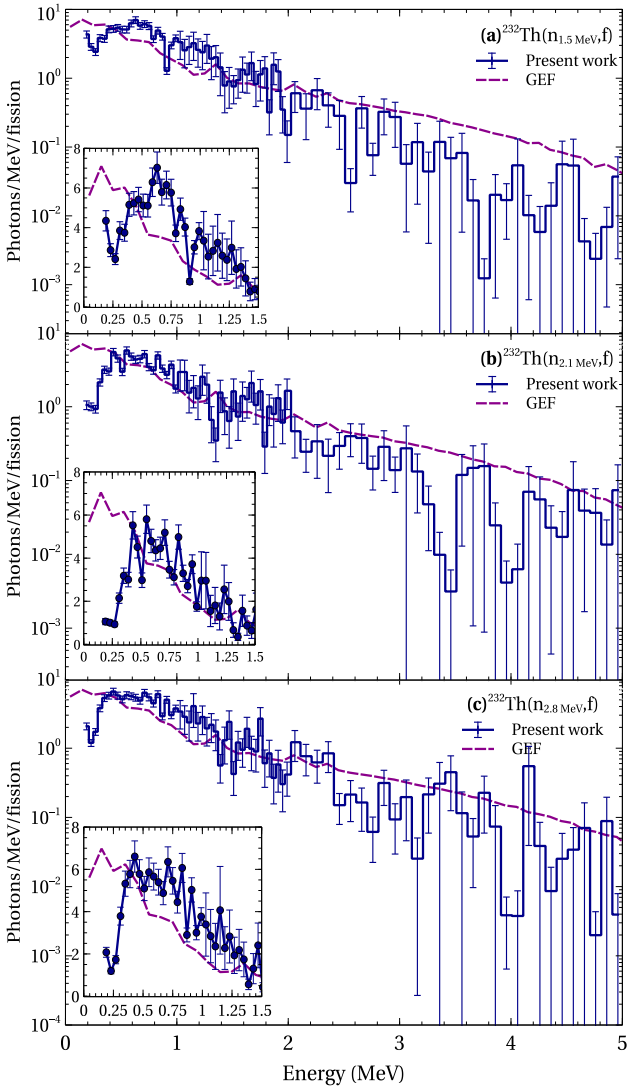

Fig. 12 The PFGS obtained from the present work for all the three incident neutron energies along with the predictions of the GEF model. The low energy regions are shown in the corresponding insets

Table 2 Comparison of average γ-ray energies obtained in the present work with the predictions of the GEF model

	Average γ-ray energy (MeV)	
Reaction	Present work	GEF model
^{232}Th($n_{1.5MeV}$f)	0.95 ± 0.03	0.98
^{232}Th($n_{2.1MeV}$, f)	1.07 ± 0.04	0.98
^{232}Th($n_{2.8MeV}$, f)	1.06 ± 0.06	0.98

3.3 Prompt fission neutron spectra (PFNS)

Figure 15 shows the 2D plot of Pulse Shape versus TOF from one of the EJ301 liquid scintillation detectors. The γ-rays and the neutrons are clearly distinguished and marked in the figure. The constant background shown in the TOF

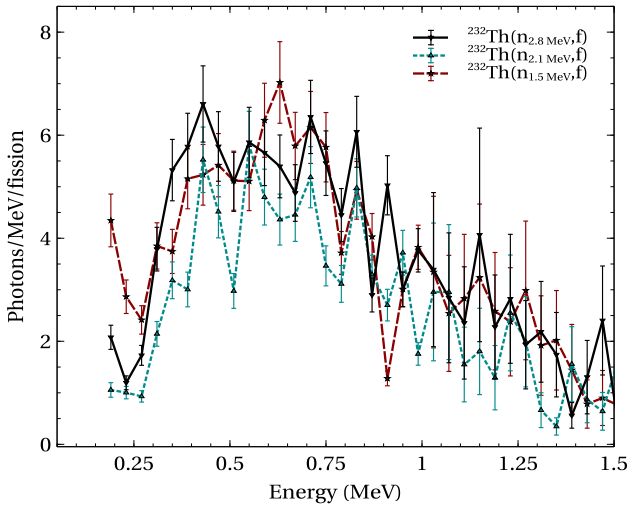

Fig. 13 Comparison of the PFGS in the low energy region, obtained from ^{232}Th(n,f) at the three incident neutron energies. The lines are inserted to guide the eyes

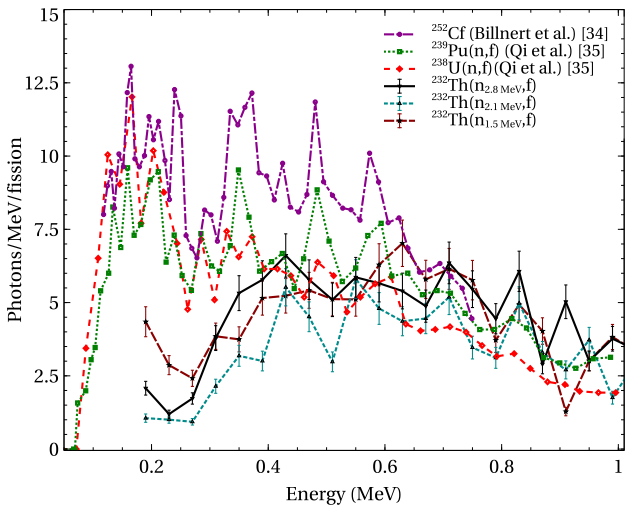

Fig. 14 Comparison of the PFGS in the low energy region, obtained from ^{252}Cf(sf) [32], ^{238}U(n$_{1.9MeV}$,f), ^{239}Pu(n$_{1.8MeV}$,f) [35] and ^{232}Th(n,f) at the three incident neutron energies. The lines are inserted to guide the eyes

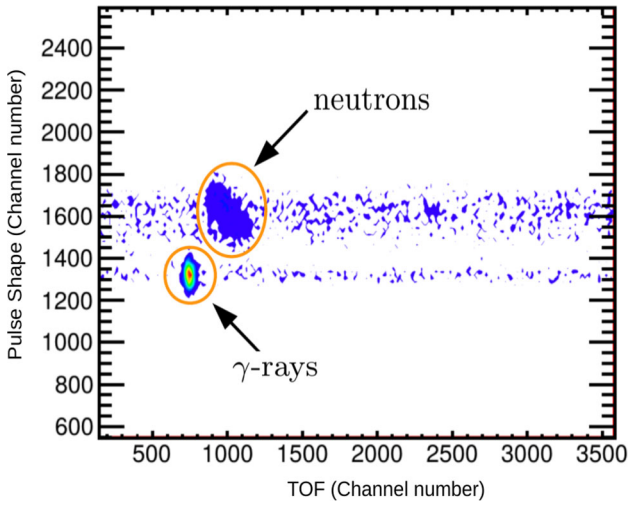

Fig. 15 The 2D plot showing Pulse Shape versus TOF of the neutrons and γ-rays for ^{232}Th(n$_{1.5\ MeV}$,f)

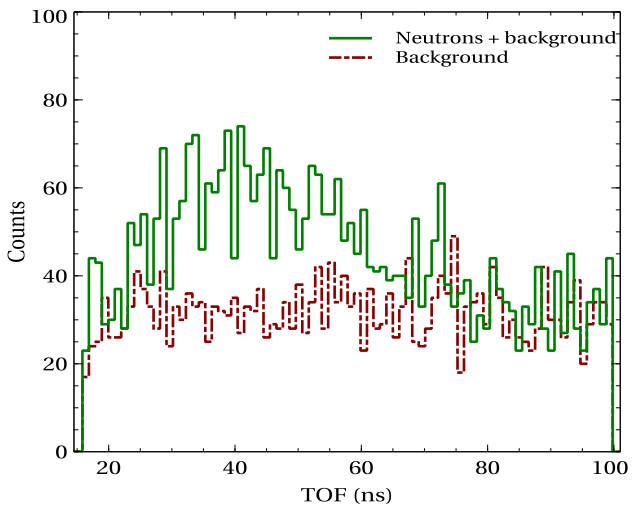

Fig. 16 Typical TOF spectrum recorded in one of the EJ301 detectors

spectra in Fig. 15 is due to the random coincidences formed by scattered background neutrons. The prompt fission neutron spectrum and the random background are shown in Fig. 16. The TOF spectra were converted into the corresponding energy spectra after appropriate calibration of the TDC channels. The energy spectrum of the background of width similar to the prompt neutron coincidence region in the TOF spectrum (Fig. 16) was then subtracted from the measured prompt neutron energy spectrum. The neutron detection efficiencies for both the liquid scintillation detectors were obtained using Monte Carlo simulations using GEANT4 with the physics list QGSP_BIC_HP, which is well suited for neutron energies below 20 MeV [38]. The simulated efficiency curves for both the detectors (66 keVee and 47 keVee thresholds) are shown in Fig. 17. The PFNS obtained for ^{252}Cf (sf) using the EJ301 detectors after efficiency correction is shown in Fig. 18 along with the Mannhart evaluated data [37]. It can be seen that our experimentally measured efficiency corrected spectra and the Mannhart evaluated data are consistent with each other. The efficiency corrected neutron energy spectra for both the detectors were added and are plotted in Fig. 19a–c for all the three incident neutron energies. An overall time resolution(FWHM) of ∼6.7 ns was deduced from the fission prompt γ-ray peak in the TOF spectrum. The associated error on the detected neutron energy ranged from 20% at 0.78 MeV to 39% at 5.48 MeV.

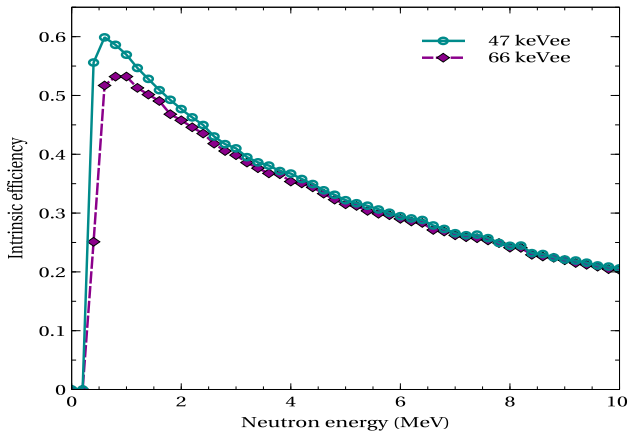

Fig. 17 Efficiency curves for the neutron detectors simulated using GEANT4. The lines are inserted to guide the eyes

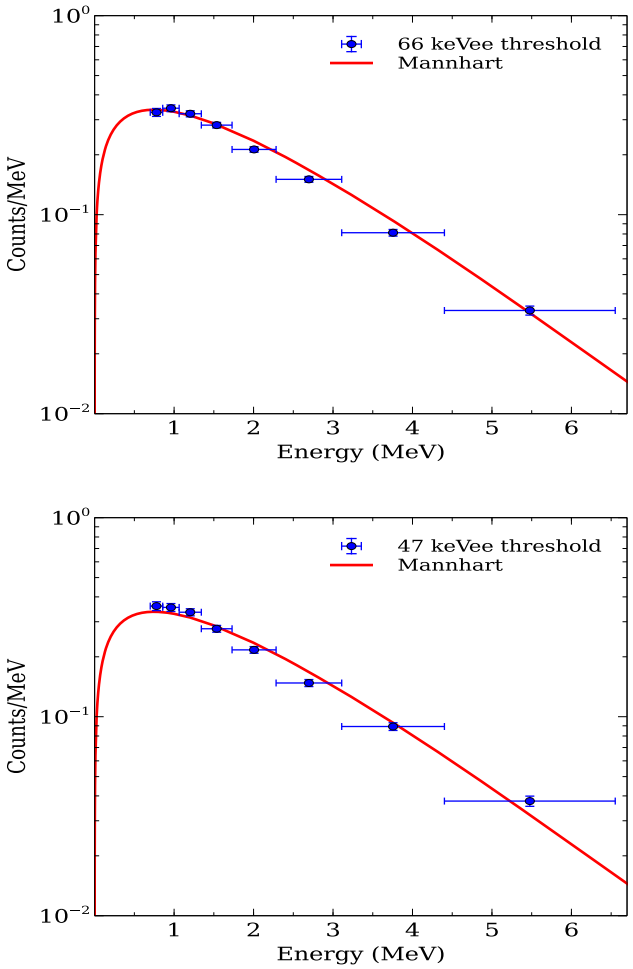

Fig. 18 PFNS obtained for ^{252}Cf (sf) in the EJ301 detectors kept at 66 keVee threshold (top) and at 47 keVee (bottom) after efficiency correction using the efficiency curves shown in Fig. 17 along with the comparison with the Mannhart evaluated data [37]

A commonly used approximation for prompt fission neutron spectra is the Maxwellian distribution [39,40], given as:

$$N_M(E) = \frac{2\sqrt{E}}{\sqrt{\pi} T_M^{3/2}} \exp(-E/T_M) \quad (1)$$

where T_M is the Maxwellian temperature and E is the neutron energy (in MeV). The average neutron energy is given by:

$$\bar{E}_n = \frac{3}{2} T_M \quad (2)$$

In the lab frame, the Maxwellian distribution transform into a Watt spectrum [41,42] given by:

$$N_W(E) = \frac{2A^{3/2}}{(\pi B)^{1/2}} \times \exp\left(-\frac{B}{4A}\right) \times \exp(-A.E) \times \sinh(B.E)^{1/2} \quad (3)$$

Watt parameters A and B are related to the physical quantities by the relations: A=1/T_e and B=4E_f/T_e^2. Here, T_e is the temperature of the nucleus after the evaporation of one neutron and it is assumed that all fragments have the same kinetic energy per nucleon E_f. The average neutron energy from Watt distribution is given by:

$$\bar{E}_n = \frac{1}{A}\left(\frac{3}{2} + \frac{B}{4A}\right) \quad (4)$$

The experimental data fitted with the Maxwellian distribution (red solid line) and Watt distribution (blue dashed line) are shown in Fig. 19a–c for incident neutron energies of 1.5, 2.1 and 2.8 MeV. Consistent results were obtained using Watt and Maxwell distributions. In order to estimate the error due to background subtraction, TOF spectrum for prompt fission neutrons obtained from ^{252}Cf(sf) was simulated using GEANT4-FREYA by keeping the same signal to background ratio as that observed in the experiment. Aforementioned background subtraction technique was then used to obtain T_M for ^{252}Cf(sf). It was then compared with T_M obtained from a GEANT4-FREYA simulation carried out with no background noise for similar number of events. Average deviation in Maxwellian temperatures extracted with and without any background in the case of ^{252}Cf(sf) was then used to calculate the error in case of ^{232}Th(n,f). This along with the fitting error yielded the total error in extracted parameters T_M, A and B. Table 3 shows the Maxwellian temperature, the average neutron energy from Maxwellian and Watt distribution obtained in the present work along with their values predicted by the GEF model.

From the data available in literature [28,43], the T_M values for the fast neutron induced fission of ^{232}Th at different incident neutron energies along with the present measurement are shown in Fig. 20. The GEF model predicts a slowly rising Maxwellian temperature from 1.23 to 1.29 MeV as incident neutron energy increases from 1 to 5 MeV (solid line). It can be seen that the value of T_M obtained from the present work is in reasonable agreement with the predictions of the GEF model. However, more accurate measurements with much reduced background are desirable to conclusively establish the excitation energy dependence of the PFNS.

Table 3 Comparison of neutron spectral characteristics obtained in the present work with the predictions of the GEF model

Reaction	Maxwellian temperature (MeV)		$\bar{E}_n$ (Maxwell) (MeV)		Watt parameters		$\bar{E}_n$(Watt)(MeV)
	Present work	GEF	Present work	GEF	A (MeV^{-1})	B (MeV^{-1})	
^{232}Th($n_{1.5MeV}$,f)	1.28 ± 0.10	1.23	1.93 ± 0.14	1.85	1.11 ± 0.32	2.84 ± 0.06	1.92 ± 0.72
^{232}Th($n_{2.1MeV}$,f)	1.16 ± 0.09	1.24	1.73 ± 0.14	1.86	1.21 ± 0.06	2.87 ± 0.05	1.73 ± 0.11
^{232}Th($n_{2.8MeV}$,f)	1.25 ± 0.09	1.26	1.87 ± 0.14	1.89	1.13 ± 0.04	2.77 ± 0.08	1.86 ± 0.09

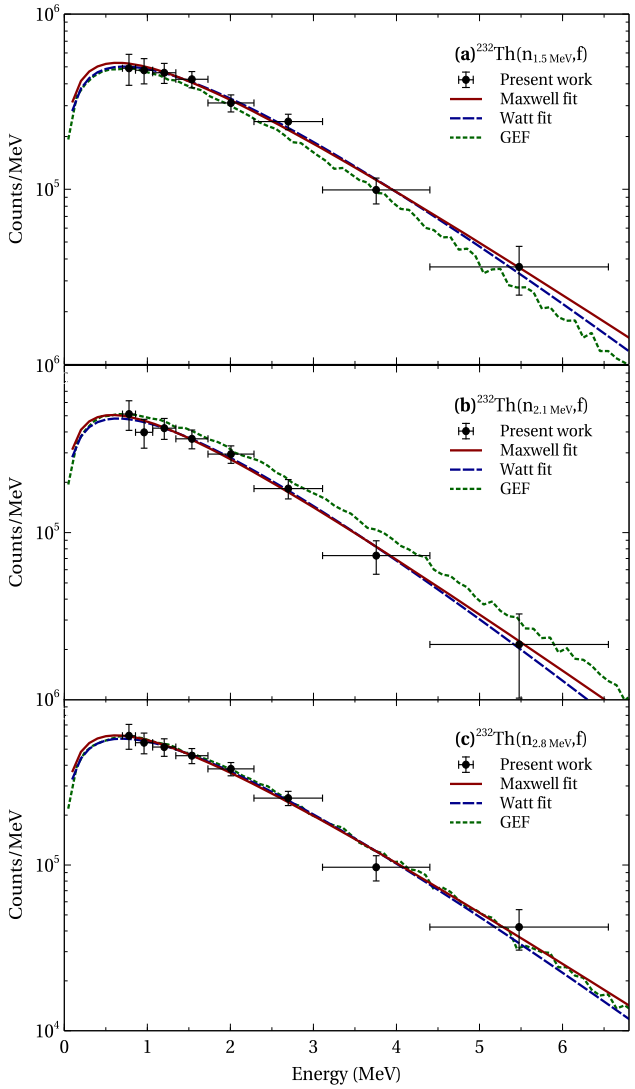

Fig. 19 The experimental PFNS fitted with the Maxwellian and Watt distributions and comapred with the GEF prediction for ^{232}Th(n,f)

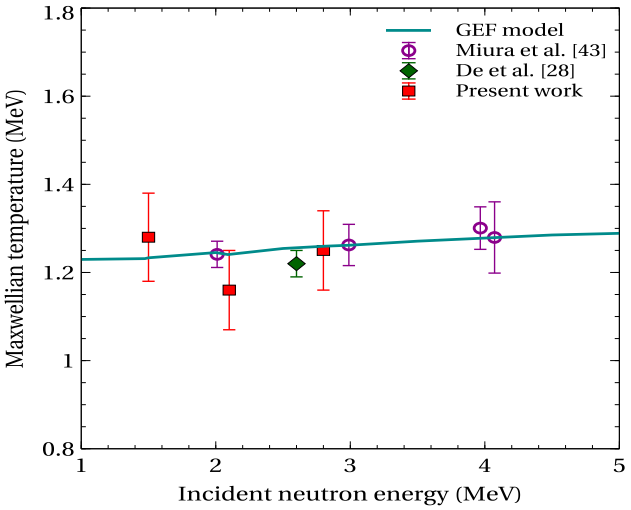

Fig. 20 Maxwelllian temperature(T_M) as a function of incident neutron energy

4 Summary

Prompt fission γ-rays and neutrons have been measured for the ^{232}Th(n,f) reaction at near and above the threshold energies, 1.5 MeV, 2.1 MeV and 2.8 MeV, using quasi monoenergetic neutrons produced via ^{7}Li(p,n)^{7}Be reaction. The γ-rays were recorded using two $CeBr_3$ scintillation detectors in coincidence with a twin section fission trigger ionisation chamber while the neutrons were detected using two EJ301 liquid scintillation detectors. The energy spectra of γ-rays were obtained after unfolding the detected pulse height spectrum using the response matrix of the $CeBr_3$ detectors. While no significant excitation energy dependence for the spectral characteristics of the PFGS for ^{232}Th(n,f) has been observed, the PFGS for ^{232}Th(n,f) when compared with the existing data of ^{252}Cf(sf),^{239}Pu(n,f) and ^{238}U(n,f), showed noticeably lower intensity of photons at energies less than 0.7 MeV. It is also found that the observed γ-ray spectra of ^{232}Th(n,f) at all the incident neutron energies studied are not in good agreement with the predictions of the GEF model. The prompt fission neutron energy spectra so obtained are fitted using Maxwell distribution and Watt parametrization to derive the average prompt fission neutron energy. It is found that the average energy of the prompt fission neutrons are in reasonable agreement with the predictions of the GEF model in this incident neutron energy region. The present data will be an important addition for improving the modelling of fast neutron induced fission of actinides for the data driven models.

Acknowledgements The authors thank the FOTIA staff for their support and the smooth operation of accelerator during the experiment and

Mr. Rohan Turbhekar, Target Lab, TIFR, for providing the Lithium foils for the experiment. They are thankful to Dr. A.K. Gupta for his constant encouragement and support of this programme. They would also like to thank Dr. R.K. Choudhury and Dr. A. Saxena for fruitful discussions.

Data availability statement This manuscript has no associated data or the data will not be deposited. [Authors' comment: The authors can be contacted for the data presented in this article.]

References

1. Alf Gö̈k, Franz-Josef Hambsch, Stephan Oberstedt, and Marzio Vidali, Phys. Rev. C 98, 044615 (2018)
2. L. Thulliez, O. Litaize, O. Serot, A. Chebboubi, Phys. Rev. C **100**, 044616 (2019)
3. A. Al-Adili, D. Tarrío, K. Jansson, V. Rakopoulos, A. Solders, S. Pomp et al., Phys. Rev. C **102**, 064610 (2020)
4. Jorgen Randrup, Ramona Vogt, Phys. Rev. Lett. **127**, 062502 (2021)
5. Aurel Bulgac, Ibrahim Abdurrahman, Shi Jin, Kyle Godbey, Nicolas Schunck, Ionel Stetcu, Phys. Rev. Lett. **126**, 142502 (2021)
6. J. Wilson, D. Thisse, M. Lebois et al., Nature (London) **590**, 566 (2021)
7. I. Stetcu, A.E. Lovell, P. Talou, T. Kawano, S. Marin, S.A. Pozzi, A. Bulgac, Phys. Rev. Lett. **127**, 222502 (2021)
8. Aurel Bulgac, Ibrahim Abdurrahman, Kyle Godbey, Ionel Stetcu, Phys. Rev. Lett. **128**, 022501 (2022)
9. C. Wagemans, *The Nuclear Fission Process* (CRC, Boca Raton, 1991), pp.498–501
10. Matthew J. Marcath, Robert C. Haight, Ramona Vogt, Matthew Devlin, Patrick Talou, Ionel Stetcu et al., Phys. Rev. C **97**, 044622 (2018)
11. K.H. Schmidt, B. Jurado, C. Amouroux, C. Schmitt, Nucl. Data Sheets **131**, 107–221 (2016)
12. J.M. Verbeke, J. Randrup, R. Vogt, Comput. Phys. Commun. **222**, 263–266 (2018)
13. P. Talou, I. Stetcu, P. Jaffke, M.E. Rising, A.E. Lovell, T. Kawano, Comput. Phys. Commun. **269**, 108087 (2021)
14. O. Litaize, O. Serot, Phys. Rev. C **82**, 054616 (2010)
15. A. Chyzh, C.Y. Wu, E. Kwan, R.A. Henderson, T.A. Bredeweg, R.C. Haight, A. C. Hayes-Sterbenz, H.Y. Lee, J.M. O′Donnell and J.L. Ullmann, Phys. Rev. C 90, 014602 (2014)
16. J.L. Ullman, E.M. Bond, T.A. Bredeweg, A. Couture, R.C. Haight, M. Jandel, T. Kawano, H.Y. Lee, J.M. O′Donnell, A.C. Hayes, I. Stetcu et al., Phys. Rev. C 87, 044607 (2013)
17. A. Gatera, T. Belgya, W. Geerts et al., Phys. Rev. C **95**, 064609 (2017)
18. S. Oberstedt, A. Oberstedt, A. Gatera et al., Phys. Rev. C **93**, 054603 (2016)
19. A. Chatillon, G. Bélier, T. Granier, B. Laurent, B. Morillon, J. Taieb, Phys. Rev. C **89**, 014611 (2014)
20. K.J. Kelly, M. Devlin, J.M. O'Donnell, J.A. Gomez, D. Neudecker, R.C. Haight, T.N. Taddeucci, S.M. Mosby, H.Y. Lee, C.Y. Wu, R. Henderson et al., Phys. Rev. C **102**, 034615 (2020)
21. E. Blain, A. Daskalakis, R.C. Block, Y. Danon, Phys. Rev. C **95**, 064615 (2017)
22. N. Colonna, F. Belloni, E. Berthoumieux, M. Calviani, C. Domingo-Pardo, C. Guerrero, D. Karadimos, C. Lederer, C. Massimi, C. Paradela et al., Energy Environ. Sci. **3**, 1910–1917 (2010)
23. H. Makii, K. Nishio, K. Hirose, R. Orlandi, R. Léguillon, T. Ogawa, T. Soldner, U. Köster, A. Pollitt et al., Phys. Rev. C 100, 044610 (2019)
24. D. Gjestvang, S. Siem, F. Zeiser, J. Randrup, R. Vogt, J.N. Wilson, F. Bello-Garrote, L.A. Bernstein, D.L. Bleuel, M. Guttormsen et al., Phys. Rev. C **103**, 034609 (2021)
25. A. Sardet, T. Granier, B. Laurent, A. Oberstedt, Phys. Procedia **47**, 144–149 (2013)
26. G. Mishra, R.G. Thomas, A. Kumar, A. Mitra, S. De, S.V. Suryanarayana, B.K. Nayak, Nuclear Inst. Methods Phys. Res. A **921**, 33–37 (2019)
27. https://www.mesytec.com/products/nuclear-physics/MPD-4.html
28. S. De, G. Mishra, R.G. Thomas, A. Kumar, A. Mitra, B.K. Nayak, Eur. Phys. J. A **56**, 1–7 (2020)
29. J.W. Meadows, D.L. Smith, Argonne National Laboratory Reports, ANL 7938 Physics (1972)
30. R. Pachuau, B. Lalremruata, N. Otuka, L.R. Hlondo, L.R.M. Punte, H.H. Thanga, Nucl. Sci. Eng. **187**(1), 70–80 (2017)
31. S. Agostinelli, J. Allison, K. Amako, J. Apostolakis, H. Araujo, P. Arce et al., Nucl. Instrum. Meth. A **506**, 250–303 (2003)
32. R. Billnert, F.-J. Hambsch, A. Oberstedt, S. Oberstedt, Phys. Rev. C **87**, 024601 (2013)
33. L. Qi, M. Lebois, J.N. Wilson, A. Chatillon, S. Courtin, G. Fruet, G. Georgiev, D.G. Jenkins, B. Laurent, L. Le Meur, A. Maj, P. Marini et al., Phys. Rev. C **98**, 014612 (2018)
34. S. De, R.G. Thomas, P.C. Rout, S.V. Suryanarayana, B.K. Nayak, A. Saxena, JINST **13**, T02010 (2018)
35. L. Qi, C. Schmitt, M. Lebois, A. Oberstedt, S. Oberstedt, J. N. Wilson, A. Al-Adili, A. Chatillon, D. Choudhury, A. Gatera, G. Georgiev, A. Gö̈k, B. Laurent, A. Maj, I. Matea, S. J. Rose, B. Wasilewska and F. Zeiser, Eur. Phys. J. A (2020) 56:98
36. P. Talou, R. Vogt, J. Randrup, M.E. Rising, S.A. Pozzi, J. Verbeke, M.T. Andrews, S.D. Clarke, P. Jaffke, M. Jandel, T. Kawano et al., Eur. Phys. J. A **54**, 9 (2018)
37. A.D. Carlson, V.G. Pronyaev, R. Capote, G.M. Hale et al., Nuclear Data Sheets **110**, 3215 (2009)
38. P.C. Rout, A. Gandhi, T. Basak, R.G. Thomas, C. Ghosh et al., JINST **13**, P01027 (2018)
39. J. Terrell, Phys. Rev. **113**, 527 (1959)
40. W. Mannhart et al., *INDC(NDS)-220, 305* (International Atomic Energy Agency, Vienna, 1989), pp.305–336
41. B.E. Watt, Phys. Rev. **87**, 1037 (1952)
42. V.V. Desai, B.K. Nayak, A. Saxena, S.V. Suryanarayana, R. Capote, Phys. Rev. C **92**, 014609 (2015)
43. T. Miura, M. Baba, T. Win, M. Ibaraki, Y. Hirasawa et al., J. Nucl. Sci. Tech. Suppl. **2**, 409–412 (2002)